Experimental Investigation of Instability Wave Propagation in a Three-Dimensional Boundary-Layer Flow

H. Deyhle,* G. Höhler,* and H. Bippes*
Deutsche Forschungsanstalt für Luft- und Raumfahrt, Göttingen D-3400, Germany

Wave propagation phenomena in three-dimensional boundary-layer flows with crossflow instability were investigated experimentally. A 10-element hot-film sensor was flush-mounted on a rotatable insert in a swept flate plate with imposed favorable pressure gradient. By means of cross-spectral analysis it was possible to obtain direction and magnitude of the phase velocity and the group velocity of the traveling instability waves, thus filling a gap in the knowledge of crossflow instability characteristics. The waves were found to propagate approximately normal to the potential streamline direction, according to linear theory. Phase velocity and the resulting wavelengths also agree satisfactorily, whereas the measured direction and magnitude of the group velocity shows significant differences.

Nomenclature

c	= chord length, 0.5 m
c_{gr}	= group velocity
c_{ph}	= phase velocity
E	= voltage
F	= dimensionless frequency, $f \cdot \sqrt{v \cdot x_c}/Q_\infty^{3/2}$
f	= dimensional frequency
G_a	= power spectrum of $X_a(t)$
$G_{ab}(f)$	= cross spectrum of $X_a(t)$ and $X_b(t)$
k	= complex wave number vector, $k = (k_r, k_i)$, $\|k_r\| = 2\pi/\lambda$
Q_∞	= wind-tunnel velocity (blockage effects neglected)
Re_c	= freestream Reynolds number, $Q_\infty \cdot c/v$
$S_a(f)$	= complex spectrum of $X_a(t)$, $\int_{-\infty}^{\infty} X_a(t)e^{-i\omega t}\, dt$
Tu	= turbulence level
U_s, V_s	= wall parallel velocity components, averaged in time and spanwise direction (U_s, V_s are in the direction of x_s, y_s)
$\bar{u}_s, \bar{v}_s$	= wall parallel velocity components of stationary instability mode
u_s', v_s'	= wall parallel velocity components of traveling instability modes, rms values
$X(t)$	= time history record
x_c, y_c, z	= model fixed coordinate system, see Fig. 1
x_s, y_s, z	= potential streamline fixed coordinate system, see Fig. 1
α, β	= wall parallel components of the complex wave number vector k
$\gamma_{ab}^2(f)$	= coherence function
$\Delta\eta$	= distance between two arbitrary sensor elements
$\Delta\Theta$	= phase shift between two signals
η	= sensor fixed coordinate, see Fig. 2
Θ	= phase angle
λ	= wavelength
v	= kinematic viscosity
τ	= wall shear stress
Φ_∞	= geometric sweep angle
φ	= rotation angle of sensor array, see Fig. 2
χ	= crossflow Reynolds number, $1/v\int_0^\infty V_s\, dz$
ψ_{gr}	= direction of the group velocity relative to the potential streamline
ψ_s	= direction of the real part of wave vector k relative to the potential streamline
ω	= circular frequency, $2\pi f$

I. Introduction

THE fundamental work of Gregory et al.[1] demonstrated theoretically the existence of stationary crossflow (CF) vortices, as observed in the early experiments on swept wings.[2] Gregory et al. applied the idea of primary linear stability analysis for two-dimensional mean flows to three-dimensional flows. The velocity component in the direction of propagation of the disturbance is regarded as a two-dimensional flow for stability purposes, leading to the localized analysis based on projected mean velocity profiles. As a result, the three-dimensional boundary-layer flow becomes unstable against both stationary CF vortices and nonstationary traveling waves. The subsequent work of Arnal et al.,[3] Malik and Poll,[4] Dallmann and Bieler,[5] and Meyer and Kleiser[6] demonstrated that both instability modes may play an important role in the transition process and the most highly amplified disturbances are even traveling waves rather than stationary vortices.

The experimental investigations on a swept cylinder,[7] swept flat plates,[8-11] and swept wings[12,13] provide detailed descriptions of wavelengths and amplifications of stationary vortices as well as frequencies and growth of traveling waves. However, in most of the previous experiments, the main emphasis was placed on the development of the stationary vortices. Detailed studies on traveling waves were restricted to measurements of rms values and frequency spectra.[9,11-13]

The comparison of experimental observations and theoretical results reveals a rather contrary picture. Wavelengths of the CF vortices and frequencies of traveling waves agree satisfactorily, whereas the disturbance growth is overpredicted by local linear theory. An open question in this comparison is still the direction of wave propagation of traveling waves. Stability calculations predict the most amplified waves propagating approximately normal to the potential streamline direction.[6] The direction of propagation has also proved to be of main importance for the determination of streamline curvature effects on the disturbance growth. Moreover, the agreement of wavelengths and phase velocities of traveling waves with linear theory has not been examined so far. The present experiment is aimed at filling this gap.

A first attempt to measure the direction of wave propagation was made by Bippes and Nitschke-Kowsky[14] using a rotatable twin hot-wire probe. A preferred direction different from the direction of the potential flow was presumed to exist but could not be clearly identified. The restricted range of angular

*Scientist, Institute for Experimental Fluid Mechanics, Bunsenstraße 10.

positions of the probe to avoid extremely oblique directions toward the hot wires turned out to be a problem.

In the present investigation a multielement hot-film sensor was used (developed and distributed by AS&M, Inc.). Mangalam et al.[15] first applied these sensors in experiments on swept wings. They determined the location of the attachment line and transition region as well as wavelengths of stationary CF vortices. Traveling waves were investigated merely by means of power spectra of individual signals. In contrast to the fixed mounted sensors of Mangalam et al.,[15] the hot-film array in the present experiment was flush mounted on a rotatable insert in the flat plate. With this nonintrusive measurement technique it was possible to determine propagation directions, wavelengths, and phase velocities, as well as direction and magnitude of group velocities. The latter are of special interest for the e^n method.

II. Apparatus and Method

The present experiment was conducted in the 1-m wind tunnel of the DLR in Göttingen. It is a closed-circuit tunnel with a contraction ratio of 3.8 and a rectangular open test section of 1×0.7 m^2. The turbulence level in the test section, integrated over the spectral distribution of all of the three spatial velocity components in the range 2 Hz $\leq f \leq$ 2 kHz, is $Tu = 0.15\%$.

To simulate the accelerated three-dimensional boundary-layer flow on the front part of swept wings, a swept flat plate (chord length $c = 0.5$ m) with displacement body was designed (for details see Müller[16]). Contoured end plates were used to insure infinite swept wing conditions. In Figs. 1a and 1b the model and the used coordinate systems are shown. Because of the favorable pressure gradient (Fig. 1c), which is nearly constant on this model, the potential streamline is curved toward the wing root. Within the boundary layer the velocity profile
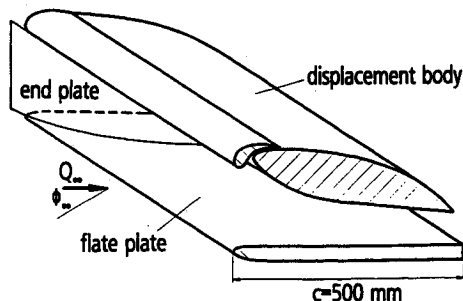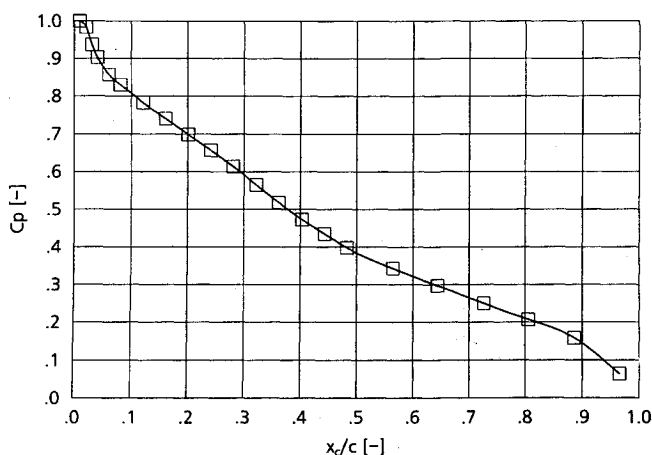
is twisted to maintain the balance of centrifugal and pressure forces (Fig. 1d). The sweep angle $\Phi_\infty = 45$ deg and the strong pressure gradient lead to crossflow instability at low freestream Reynolds numbers and provide a relatively thick boundary layer, in which quantitative measurements can be performed.[16]

The sensor was a straight-line array of 10 individual hot films, mounted on a rotatable insert in the flat plate. In Fig. 2 the sensor arrangement and the dimensions of the array are shown. Each sensor consists of a 0.25 μm thick and 0.12 mm wide nickel film with 5 μm copper-coated nickel leads. The polyimide substrate was embedded in epoxy, and the leads were routed away from the surface. This yielded to an installation without any influence on the flow. Because of damaged leads sensor element number 2 (HF2) could not be used. The rotatable insert was flush mounted in the flat plate at a fixed position $x_c/c = 0.7$ and was adjustable to arbitrary angular positions in the range $-180 \leq \varphi \leq 180$ deg. The individual sensor elements were operated at $T \approx 75°C$ using constant temperature anemometers. Only the measurement relevant sensors (max. 2) were heated to avoid interference with the flow downstream of the sensor. The voltage signals were processed without calibration on a two-channel digital spectrum analyzer.

Data processing was performed using spectral analysis. Because of the dispersive nature of boundary-layer flows, cross-spectral analysis was used instead of cross-correlation analy-
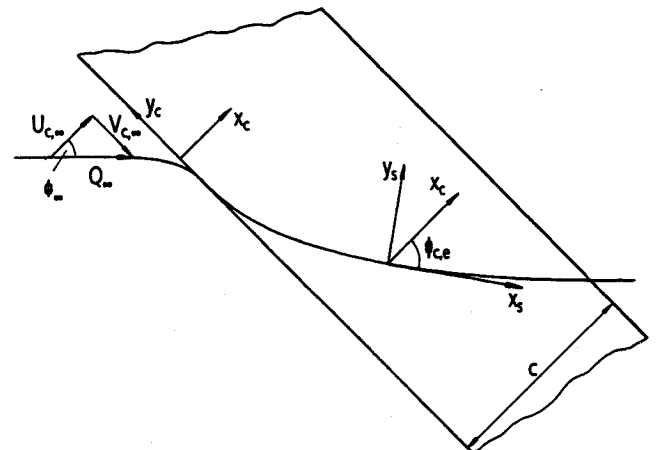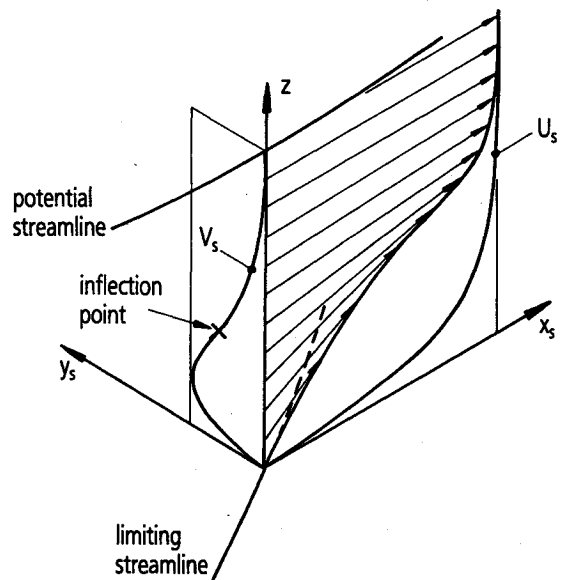

Fig. 1c　Coordinate systems on the swept flat plate.

Fig. 1a　Model of the swept flat plate with displacement body.

Fig. 1b　Pressure distribution.

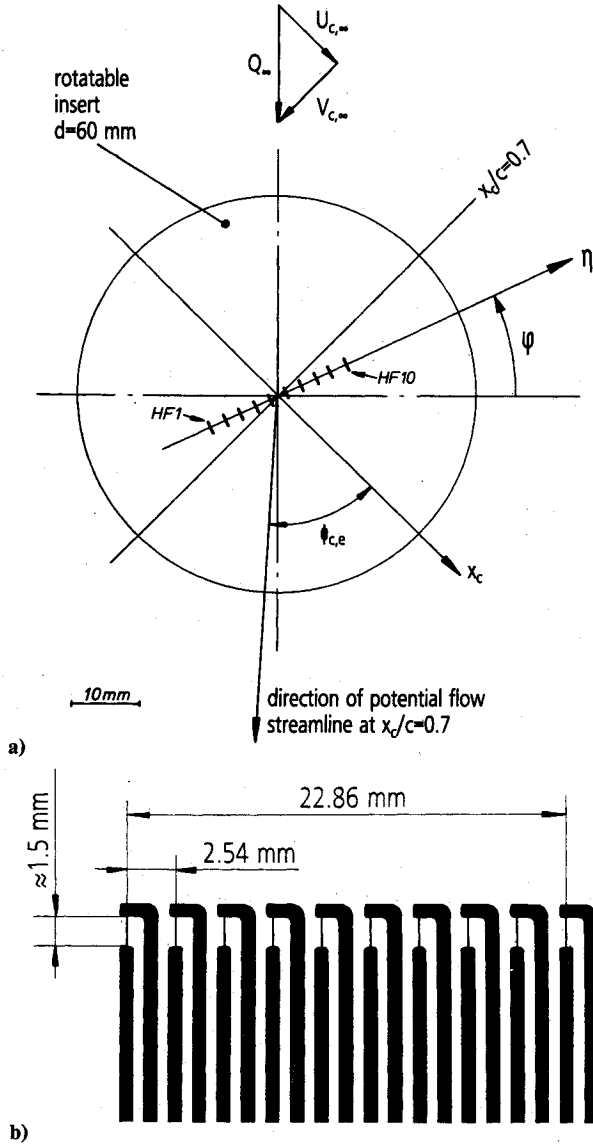Fig. 1d　Three-dimensional boundary-layer profile.

Fig. 2 Arrangement and dimensions of the 10-element sensor array (φ = rotation angle of the insert, η = sensor fixed coordinate).

sis. Hence, phase shifts and coherence are provided as functions of frequency. By means of a concrete example the processing will be explained in the following. Figure 3 displays two time history records, taken with hot-film sensor elements 6 [HF6, $X_a(t)$] and 7 [HF7, $X_b(t)$] at an angular position $\varphi = 0$ deg and a freestream velocity $Q_\infty = 19$ m/s. The traveling waves, propagating in space, manifest themselves as regular fluctuations of the bridge voltages. Because of the distance between the two sensors of $\Delta\eta = 2.54$ mm, the signal shows a phase shift $\Delta\Theta$. From the two signals the cross spectrum $G_{ab}(f) = S_b \cdot S_a^*$ is calculated with S_b and S_a^* representing the complex spectrum of $X_b(t)$ and the complex conjugate of S_a, respectively. Averaging over 20 or more data windows yields a spectral distribution as shown in Fig. 4. The upper diagram in Fig. 4 represents a plot of the coherence function γ_{ab}^2, defined as

$$\gamma_{ab}^2(f) = \frac{|G_{ab}(f)|^2}{G_a(f)G_b(f)} \qquad 0 \le \gamma_{ab}^2 \le 1 \qquad (1)$$

which displays the normalized magnitude of the cross spectrum. In the frequency range $50 < f < 150$ Hz the signals are highly coherent ($\gamma_{ab}^2 \approx 1$) due to the traveling waves. Considering the phase of the cross spectrum G_{ab} (lower diagram in Fig.

4), it becomes obvious that in the same frequency range the phase exhibits an almost linear dependence on frequency.

For the determination of the phase velocity and the group velocity by means of the cross spectrum, a single harmonic wave of frequency f, wavelength λ, and phase velocity

$$c_{ph}(f) = \frac{\omega}{k} \qquad (2)$$

is considered. With the phase shift $\Delta\Theta$ between signals of two sensors positioned a distance $\Delta\eta$ apart, the phase velocity can be determined as

$$c_{ph}(f) = 2\pi\Delta\eta \frac{f}{\Delta\Theta(f)} \qquad (3)$$

where $\Delta\Theta(f)$ can be taken from the averaged phase spectrum of $G_{ab}(f)$. Therefore, the component of the phase velocity in the direction of the sensor orientation η can be evaluated. Similarly to the phase velocity, the group velocity

$$c_{gr}(f) = \frac{d\omega}{dk} \qquad (4)$$

is given to

$$c_{gr}(f) = 2\pi\Delta\eta \frac{df}{d(\Delta\Theta)} \qquad (5)$$

where $df/d(\Delta\Theta)$ represents the inverse slope of the phase spectrum at the desired frequency f. The method to determine the still missing direction of c_{ph} and c_{gr} is described in Sec. IV.
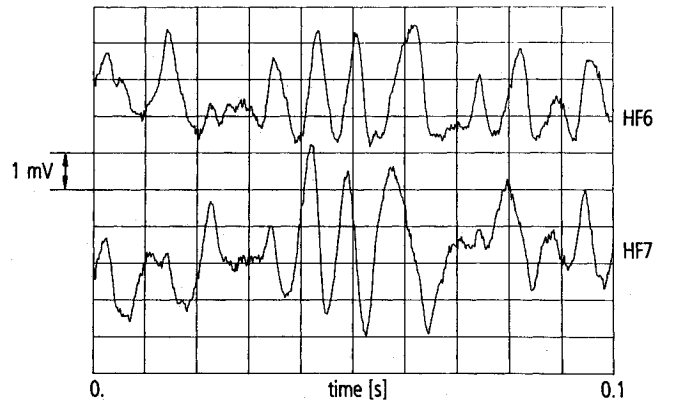

Fig. 3 Time history records of two sensor elements [$Q_\infty = 19$ m/s, $\varphi = 0$ deg, $\Delta\eta = 2.54$ mm, HF6 $= X_a(t)$, HF7 $= X_b(t)$].
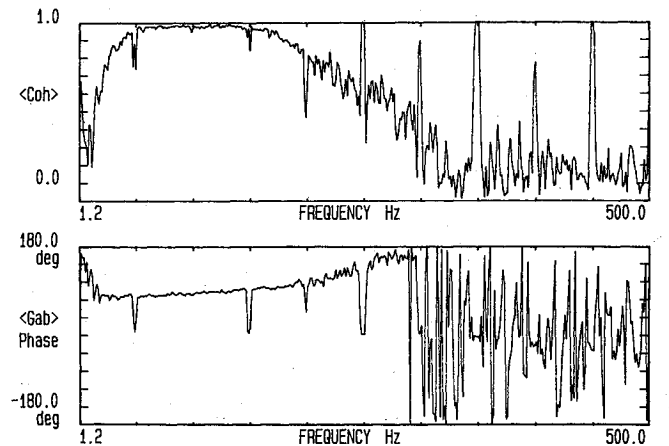

Fig. 4 Averaged coherence function γ_{ab}^2 and phase of G_{ab} for two sensor elements [$Q_\infty = 19$ m/s, $\varphi = 0$ deg, $\Delta\eta = 2.54$ mm, HF6 $= X_a(t)$, HF7 $= X_b(t)$].

III. Time-Averaged Flow

For an illustration of the disturbance development, Fig. 5 shows a typical flow pattern observed in the unstable boundary layer on the swept flat plate. The velocity distributions in a cross section at $x_c/c = 0.7$ are displayed by means of isolines. The wall parallel components of the mean flow are $(U_s + \bar{u}_s)$ and $(V_s + \bar{v}_s)$. The velocities are given in the (x_s, y_s, z) system (see Fig. 1b) and plotted over model-fixed coordinates (x_c, y_c, z). The time-averaged flow $(U_s + \bar{u}_s, V_s + \bar{v}_s)$ is deformed periodically with the wavelength of the stationary CF vortices, which are counter-rotating vortices (see the $\bar{u}_s$, $\bar{v}_s$ plots). Only because of the superposition of the mean flow (U_s, V_s) on the disturbance flow $(\bar{u}_s, \bar{v}_s)$, the pattern of

corotating vortices turns out. Another feature of this flow is the spanwise amplitude modulation of the traveling waves having the periodicity of the stationary CF vortices.

As a consequence of this flow pattern, the direction and magnitude of the wall shear stress changes periodically in the spanwise direction. In incompressible flows with constant fluid properties, hot-film sensors are sensitive to changes in the wall shear stress.[17] Therefore an output signal of a hot-film sensor, located out of the center of the rotatable insert, may be influenced by two effects. On one hand, the mean bridge voltage changes due to the rotation of the sensor element, i.e., the directional sensitivity. On the other hand, the changed position within the spanwise varying shear stress results additionally in a variation of the bridge voltage. This is demon-
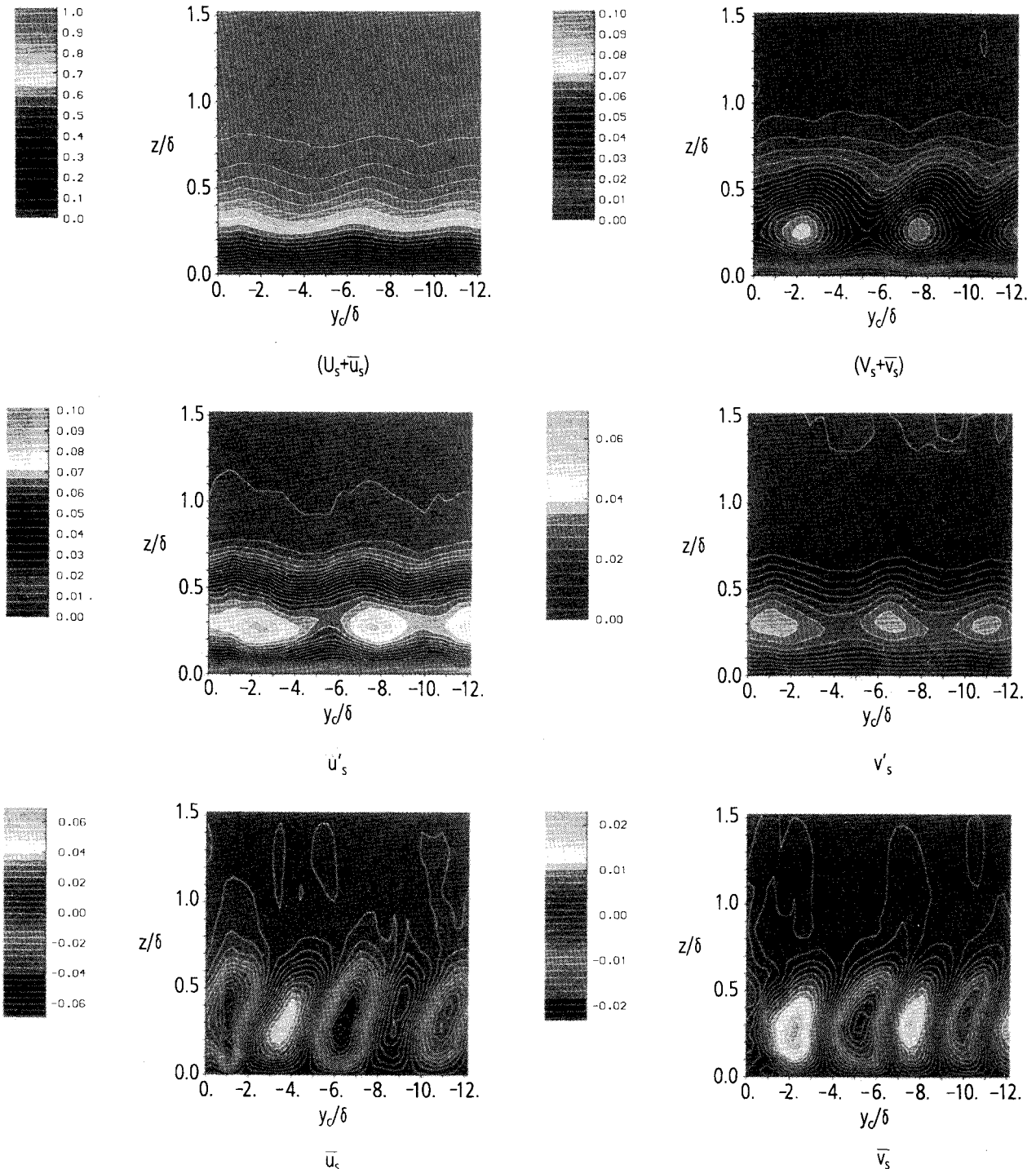

Fig. 5 Isocontours of the streamwise and crossflow components of the mean flow $(U_s + \bar{u}_s, V_s + \bar{v}_s)$, of the rms values of the traveling instability mode (u'_s, v'_s), and of the stationary instability mode $(\bar{u}_s, \bar{v}_s)$ in a cross section $x_c/c = 0.7$. All of the velocity components are nondimensionalized by the mean velocity at the outer edge of the boundary layer.

strated in Fig. 6, which displays the variation of the mean bridge voltage dependent on the angular position φ for two sensor elements. Hot-film number 6 (HF6) is located only 1.27 mm from the center of rotation. Hence this curve shows solely the expected directional sensitivity with a rather distinct maximum at $\varphi \approx -80$ deg. At this angular position, the coordinate η represents the direction of the wall shear stress. However, HF10 is located 11.43 mm apart from the center and displays two maxima of the mean voltage at $\varphi \approx -80$ and -120 deg, due to superposition of directional sensitivity and shear stress variations. At the minima of the curves, the signal/noise ratio is considerably lower than in the maxima, and therefore the uncertainty of the measurement increases. This could be of influence on the determination of the properties of traveling waves.

As already mentioned, Mangalam et al.[15] measured wavelengths of stationary CF vortices. Their method must assume that either the stationary vortices undergo a slight meandering motion or the traveling waves of low frequencies interact with the CF vortices. In the present investigation, a similar test was performed, although the spatial resolution and the total length of the 10-element sensor are far too low to determine the wavelength accurately. Whereas in Ref. 15 phase shifts $\Delta\Theta$ between sensor elements with a constant separation of 1.5 mm had been considered, in this experiment additionally the phase shift between HF10 and all of the other elements was measured. This second procedure turned out to be the more effective. The sensor array was positioned at $\varphi = 45$ deg parallel to the leading edge. Merely frequencies $f < 2$ Hz were taken into account (Mangalam et al.[15]: $f < 10$ Hz). In Fig. 7 the phase of
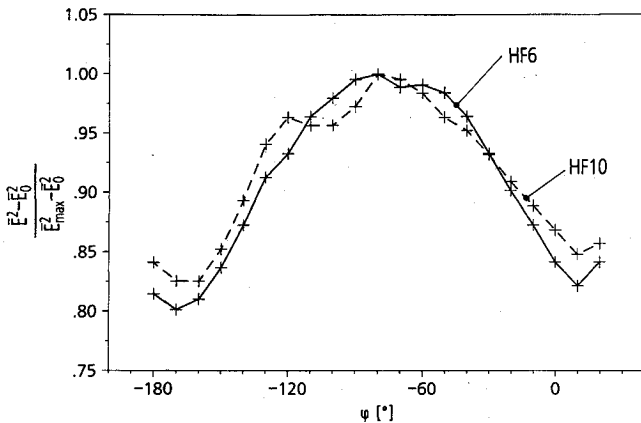

Fig. 8 Phase shifts for frequencies $f \leq 2.0$ Hz, measured by means of the cross spectrum between HF10 and all the other sensor elements [$Q_\infty = 19$ m/s, $\varphi = 45$ deg, HF10 $= X_a(t)$, HF1 $\cdots$ HF9 $= X_b(t)$].

Fig. 9 Spanwise distribution of mean bridge voltage, measured by a hot-wire probe traversed in y_c direction for two different test runs ($Q_\infty = 19$ m/s, $z/\delta \approx 0.3$, hot-film sensor array indicated in the figure corresponds to $\varphi = 45$ deg).

Fig. 6 Variation of mean bridge voltage $\bar{E}(\varphi)$ for two sensor elements HF6 and HF10 ($Q_\infty = 19$ m/s, ordinate is proportional to $\tau^{1/3}$).

G_{ab} illustrates the occurrence of 180-deg phase shifts (HF10-HF9, Fig. 7a) or in-phase signals (HF10-HF5, Fig. 7b) in this low-frequency range. To obtain the wavelength of the CF vortices, the measured phase shifts are plotted in Fig. 8. The values of $\Delta\Theta$ for discrete frequencies $f < 2$ Hz scatter considerably, indicated by error bars. Nevertheless the 180-deg shifts occur periodically at a distance between four and six times the sensor spacing $\Delta\eta$. The corresponding range of wavelengths is $10 < \lambda_c < 15$ mm and covers the spatially averaged value $\bar{\lambda}_c = 14.1$ mm as measured by Deyhle and Bippes.[18]

The actual vortex structure at the location of the sensor array was investigated also by hot-wire anemometry. A single hot-wire probe was traversed parallel to the leading edge (y_c direction), and the time-averaged bridge voltage ($\bar{t} = 6$ s) was recorded. In Fig. 9 the corresponding structure of the mean flow, deformed by CF vortices, can be seen. The two curves in this figure denote different test campaigns (test runs); in between the model was cleaned. This cleaning changed the spanwise position of stationary vortices that are initialized in this "natural" transition experiment by small surface roughnesses. The structure of $\bar{E}(y_c)$ indicates the different locations of the vortices in both runs.

IV. Traveling Waves

Primary linear stability analysis, to which the experimental results in this section are compared, still provides the basis for the most accepted engineering method to predict transition, the e^n method. Stability calculations are mostly performed using temporal amplification theory. In this case α and β
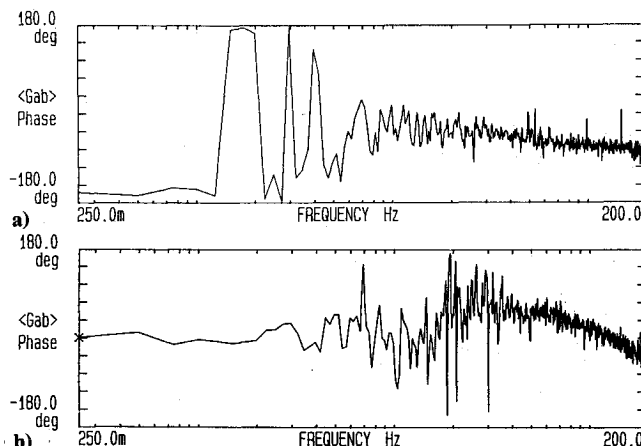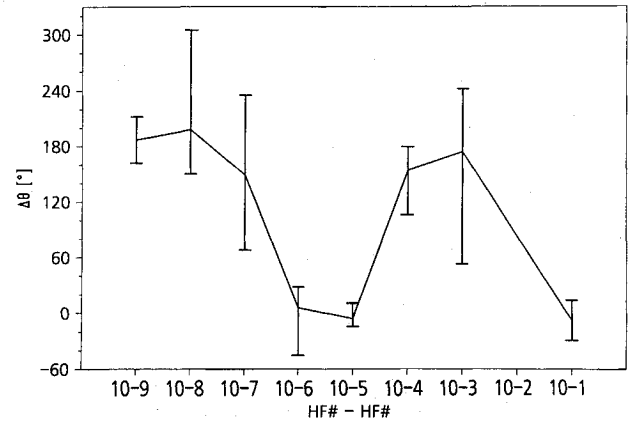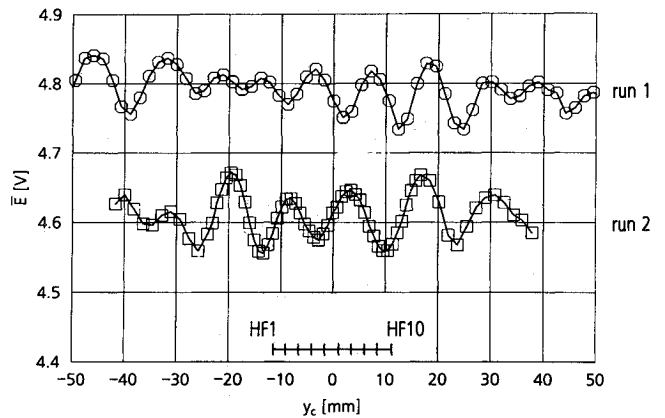

Fig. 7 Phase of G_{ab} for two different sensor spacings ($Q_\infty = 19$ m/s, $\varphi = 45$ deg): a) HF10-HF9, $\Delta\eta = 2.54$ mm, and b) HF10-HF5, $\Delta\eta = 12.7$ mm.

represent the real components of the wave vector k and the complex frequency ω. To obtain spatial amplification rates, the temporal rate ω_i is transformed using the group velocity.[19] Hence, the direction and magnitude of c_{gr} are of great importance for the evaluation of n factors. In the present experiment the direction of wave propagation $\psi_s = \arctan(\beta_r/\alpha_r)$, the phase velocity c_{ph}, the wavelength $\lambda = 2\pi(\alpha_r^2 + \beta_r^2)^{-\frac{1}{2}}$, the group velocity c_{gr}, and its direction $\psi_{gr} = \arctan[(\partial\omega_r/\partial\beta_r)/(\partial\omega_r/\partial\alpha_r)]$ are determined for different modes and compared to results from the LISA*T calculations of Meyer and Kleiser[6] (local temporal theory, neglecting curvature effects).

The freestream velocity was chosen to $Q_\infty = 19$ m/s. This corresponds to a freestream Reynolds number $Re_c = 6.3 \times 10^5$ and a crossflow Reynolds number $\chi \approx 140$ at $x_c/c = 0.7$. The 99.9% thickness and the displacement thickness of the boundary layer at this streamwise position are 2.9 and 0.7 mm, respectively. In Fig. 4, the frequency range $50 < f < 150$ Hz was identified as traveling waves in good agreement with the stability calculations. Waves of frequency 60, 100, and 140 Hz were selected from this range to determine the properties of wave propagation.

Essentially there exist two possibilities. On the one hand the sensor array can be rotated until $\Delta\Theta = 0$ for the desired frequency to be detected. Then the wave propagation vector k_r is oriented normal to the sensor axis η, assuming that the wavelengths are larger than the sensor spacing and the wave fronts of the traveling modes are curved not much more than the axes of the stationary vortices. Turning the sensor by 90 deg and measuring the phase shift can be used to calculate c_{ph}. Unfortunately, in the specific case of the present experiment, this direction is approximately normal to the wall shear stress direction, i.e., low signal/noise ratio, and therefore the determination of $\Delta\Theta$ is rather uncertain. Moreover the rotation angle for $\Delta\Theta = 0$ turned out to be not clearly distinguishable. Hence another procedure was chosen. For different sensor angles in the range $-90 < \varphi < 90$ deg, which covers all possible directions, the averaged phase spectrum of G_{ab} was recorded, and for the desired frequencies the phase shifts were taken from the smoothed curves $\Delta\Theta(f)$. With $\Delta\Theta$ the component of the phase velocity in direction η was evaluated by means of Eq. (3) and plotted in polar coordinates. Figure 10 displays a
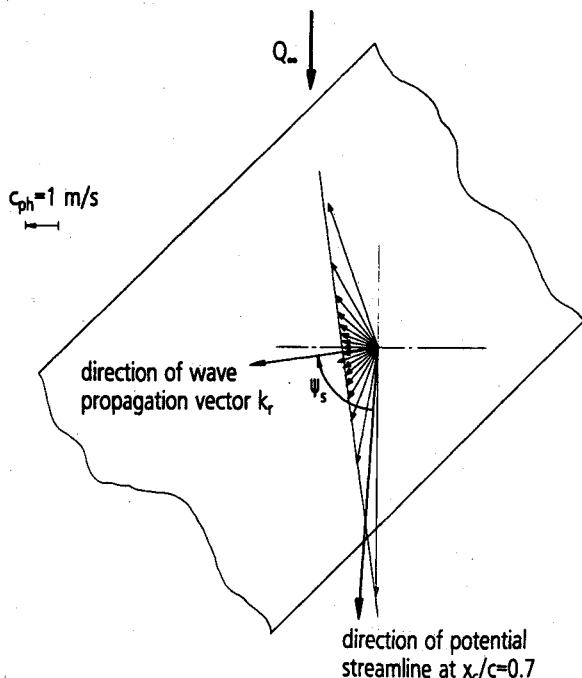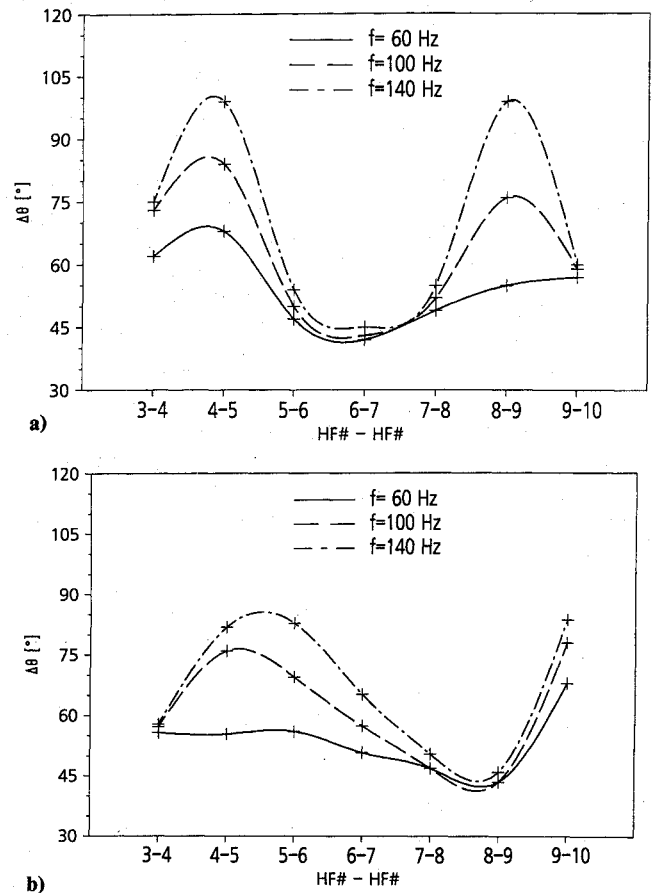

Fig. 11 Spatial variations of phase shifts, measured by different pairs of sensor elements for three frequencies in different test runs ($Q_\infty = 19$ m/s, $\varphi = 45$ deg): a) test run 1, and b) test run 2.

typical example for $f = 100$ Hz. The line, passing through all of the arrowheads of the phase velocity vectors, represents a line of constant phase or a wave front. The direction of wave propagation and the magnitude of c_{ph} in this specific direction were calculated by fitting a straight line to obtain the wave front. The accuracy of this procedure turned out to give satisfactory results, as can be checked in Fig. 10.

To get more insight into the influence of the varying shear stress on the propagation phenomena, cross spectra at different spanwise locations were compared. For $\varphi = 45$ deg the measured phase shifts between different pairs of adjacent sensor elements display considerable differences (Fig. 11). In spite of the poor spatial resolution, a periodicity of the phase shift with the wavelength of the stationary CF vortices appears. Hence, the wavelength of stationary vortices can also be determined by measuring $\Delta\Theta$ in the frequency range of traveling waves, alternatively to the procedure described in the last section. In the two different runs of the experiment (Figs. 11a and 11b), the different vortex structures turn out to be in agreement with the hot-wire measurements. It is supposed that, due to disturbance interaction, magnitude and direction of the phase velocity of the primary traveling modes are already influenced by the CF vortices. Therefore the determined directions for sensor elements, located out of center of the insert, represent merely spatially averaged values of c_{ph} because of the changed spanwise position during rotation. For a detailed investigation of these disturbance interaction phenomena, a hot-film array with individually rotatable and shiftable sensor elements would be desirable.

In Fig. 12a the measured directions of wave propagation relative to the potential streamline are plotted. The direction of k_r relative to the potential flow direction is denoted by ψ_s. The direction of the potential streamline was taken from the Falkner-Skan-Cooke (FSC) approximation. This similarity so-
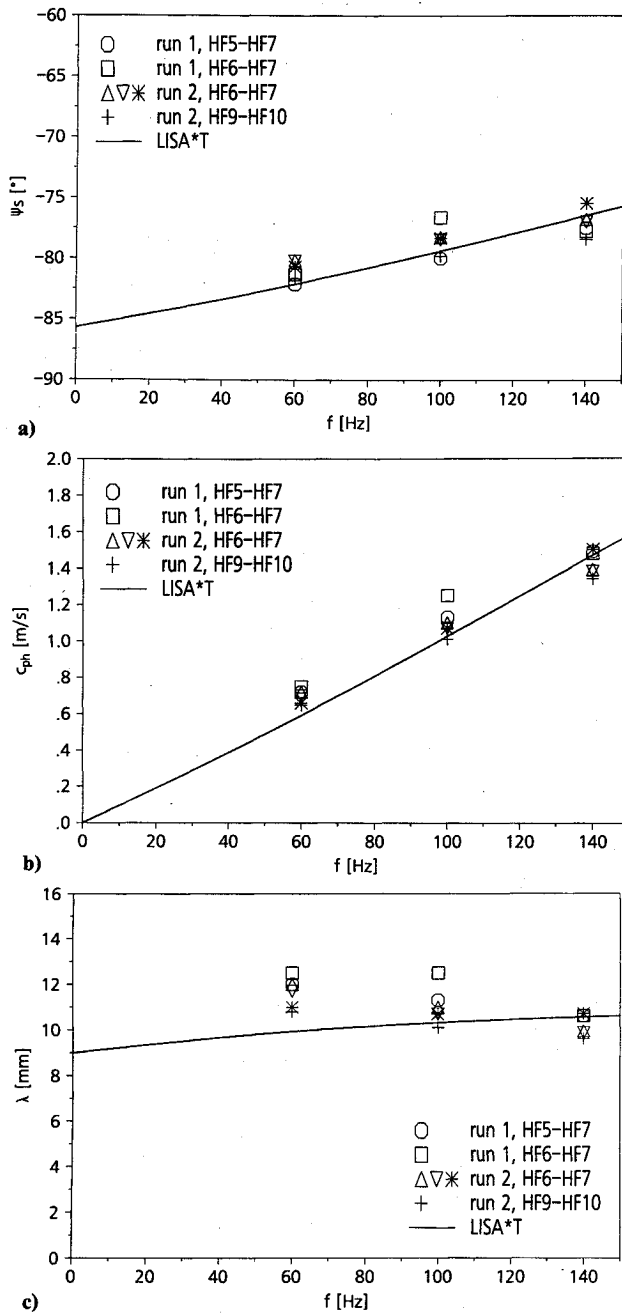

Fig. 10 Components of the phase velocity, measured in the direction of the sensor orientation for different rotation angles φ, and fitted line of constant phase for $f = 100$ Hz ($Q_\infty = 19$ m/s, run 2, sensor elements HF6-HF7).

Fig. 12 Wave propagation for f = 60, 100, and 140 Hz, measured by different pairs of sensor elements at Q_∞ = 19 m/s: a) direction of wave propagation relative to the direction of the potential streamline, b) magnitude of the phase velocity, and c) wavelength.

calculations and the decreasing tendency with increasing frequency is due to the measured phase velocities.

The determination of direction and magnitude of the group velocity is performed in a similar manner using Eq. (5). The differentiation of $\Delta\Theta(f)$ causes higher uncertainties. This was compensated to some extent by using sensor elements of larger
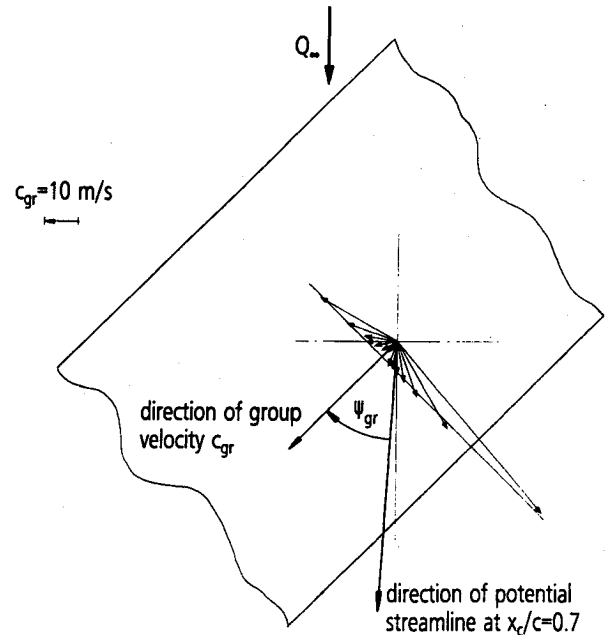

Fig. 13 Components of the group velocity for f = 100 Hz, measured in direction of the sensor orientation for different rotation angles φ (Q_∞ = 19 m/s, run 2, sensor elements HF7-HF10).

Fig. 14 Group velocity for f = 60, 100, 140 Hz at Q_∞ = 19 m/s: a) direction of the group velocity relative to the direction of the potential streamline, and b) magnitude of the group velocity.

lution was found to reproduce very closely the boundary-layer profiles on the swept flat plate model and was used for the LISA*T calculation.[6] Different pairs of sensor elements were considered to determine the influence of the vortex structure. It turns out that these differences are compensated by the described procedure. The determined directions for each frequency collapse in a very narrow range of ± 2 deg. This is also approximately the uncertainty of the procedure. Not only the magnitude of ψ_s but also the tendency of decreasing deviations from the potential streamline direction with increasing frequency agree very well with linear theory.

Figure 12b compares the determined phase velocities with LISA*T results. Again theoretical and experimental data agree well. The wavelengths of the traveling waves were calculated by $\lambda = c_{ph}/f$. The resulting values (Fig. 12c) are slightly higher than the most amplified wavelengths of the stability

Fig. 15   Averaged phase of G_{ab} and coherence function γ^2_{ab} for different freestream velocities [$\varphi = 0$ deg, HF6 $= X_a(t)$, HF7 $= X_b(t)$]: a) and b) $Q_\infty = 14$ m/s $Re_c = 4.7 \times 10^5$; c) and d) $Q_\infty = 19$ m/s $Re_c = 6.3 \times 10^5$; and e) and f) $Q_\infty = 23$ m/s $Re_c = 7.6 \times 10^5$.
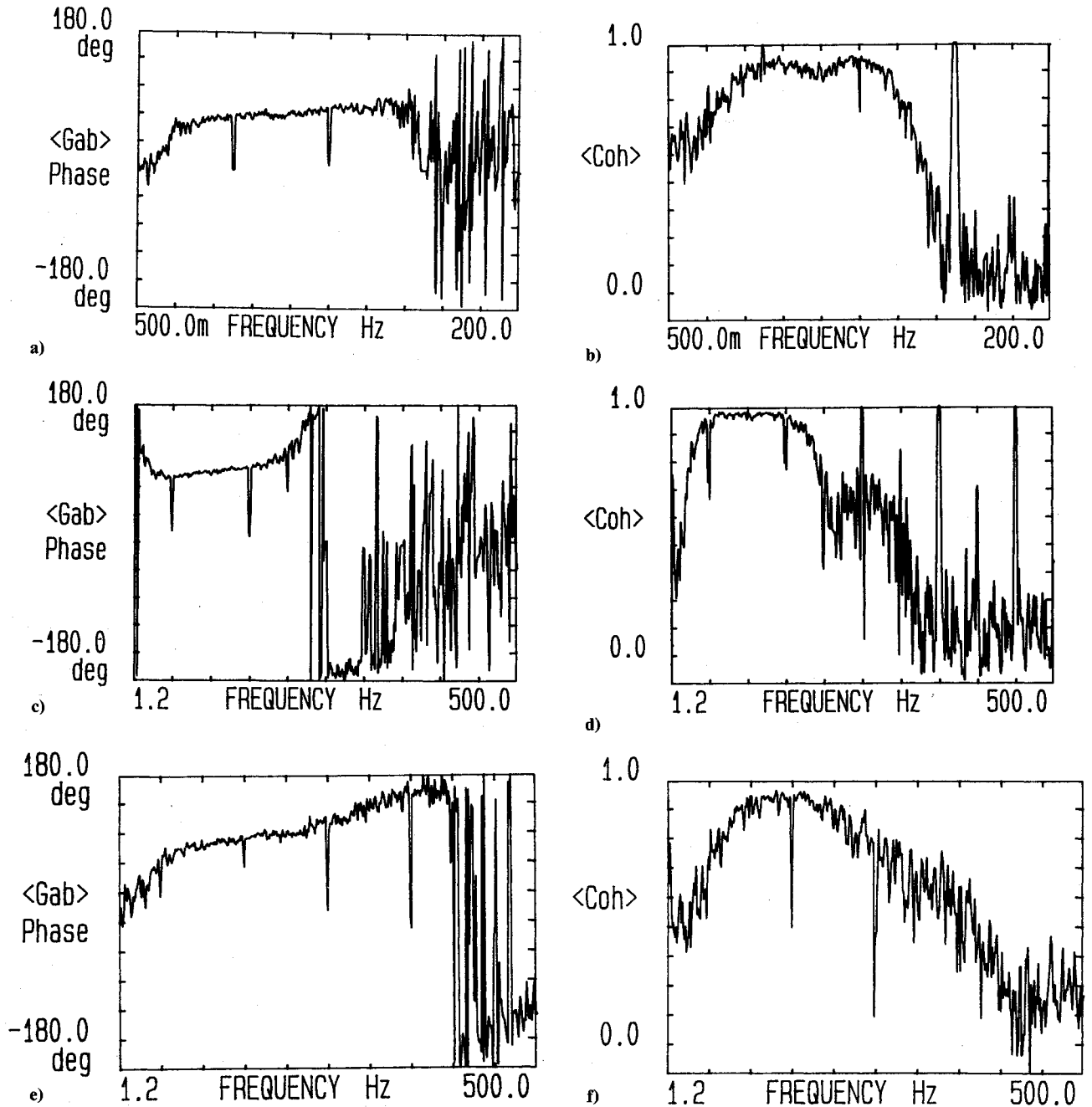
spacing ($\Delta\eta = 7.62$ mm). Nevertheless the uncertainty remains higher than for the phase velocity, as can be seen in Fig. 13 for $f = 100$ Hz. But a distinct direction of the group velocity can be obtained. In Fig. 14a the measured direction of c_{gr} is compared with the direction of the real part of the group velocity, calculated by LISA*T. The deviation from the stability calculation is in the order of 30–40 deg, whereas the experimental data scatter about 15 deg. The magnitude of c_{gr} in Fig. 14b shows lower values than the LISA*T calculated real part of the group velocity, which is used by Meyer and Kleiser[6] to determine n factors from temporal amplification rates. An explanation for this significant difference to linear theory was not found yet.

An important question in context with the traveling waves is the spatial coherence. It gives an idea of the extension of wave fronts and whether there are point sources rather than plane waves as assumed by linear theory. Measurements with sensor elements HF1 and HF10 ($\Delta\eta = 22.86$ mm) indicated a strong

coherence of $\gamma^2_{ab} > 0.98$ in the frequency range of traveling waves, as long as the signal/noise ratio was sufficient. Hence, measurements at larger distances would be possible using an array with individually rotatable sensor elements, as mentioned already. Then additionally the determination of wave front curvature would be feasible. With the currently used sensor array, this question could not be answered.

The dependence of wave propagation on Reynolds number was also investigated. Therefore the determination of ψ_s, c_{ph}, and λ was performed at $Q_\infty = 14$ m/s ($Re_c = 4.7 \times 10^5$) and at $Q_\infty = 23$ m/s ($Re_c = 7.6 \times 10^5$) additionally. The velocities were chosen to still obtain signals of measurable size ($Q_\infty = 14$ m/s) and to avoid any intermittency ($Q_\infty = 23$ m/s). In Fig. 15 the measured coherence and phase of G_{ab} are compared for the three freestream velocities. The frequency range of almost linear relation $\Delta\Theta(f)$ exists in the considered range of Q_∞ and shifts with Reynolds number. To count for the shift, the wave properties were determined at the same dimensionless frequen-

Table 1 Propagation directions, phase velocities, and wavelengths of traveling waves for three frequencies at different freestream velocities

Q_∞, m/s	$F[-]$	1.671×10^{-3}	2.785×10^{-3}	3.899×10^{-3}
14	f, Hz	37.9	63.2	88.4
	ψ_s, deg	-80.1	-79.4	-77.9
	c_{ph}, m/s	0.67	0.87	1.20
	λ, mm	17.7	13.8	13.6
19	f, Hz	60	100	140
	ψ_s, deg	-79.4	-77.5	-76.0
	c_{ph}, m/s	0.69	1.06	1.37
	λ, mm	11.5	10.6	9.8
23	f, Hz	79.8	133	186
	ψ_s, deg	-78.6	-77.9	-76.7
	c_{ph}, m/s	1.00	1.40	1.80
	λ, mm	12.5	10.5	9.7

cies F as in the $Q_\infty = 19$ m/s case. The results are given in Table 1. Although the direction of propagation was not affected very much, the wavelengths grow with decreasing Reynolds number. This is comparable to results of stability calculations for stationary CF vortices at $Re_c = 4.7 \times 10^5$, indicating also an increase of wavelength with decreasing Re_c.[20] Considering the measurements of Bippes and Nitschke-Kowsky,[14] the higher wavelengths of traveling waves at lower velocities explain the fact that Bippes and Nitschke-Kowsky could not find a zero time shift in their cross correlation at smaller Reynolds numbers. In this case the distance between the two hot wires was smaller than the wavelengths, resulting in a minimum but nonzero time shift.

V. Conclusions

The propagation of traveling waves in crossflow-induced transition is an important aspect in the verification of primary linear stability theory. Because of the applied surface hot-film technique, it was possible in the present experiment to determine nonintrusively propagation directions, wavelengths, phase velocities, and group velocities. For this purpose the sensor array was flush mounted on a rotatable insert at a fixed position in the swept flat plate. By means of cross-spectral analysis, the desired properties of wave propagation were obtained as a function of frequency. The experimental data are compared with results from temporal linear theory.

The method to determine the direction of the wave propagation vector turned out to provide satisfactory results, although an interaction between stationary CF vortices and traveling waves occurred. The propagation directions agree very well with results from linear theory. Also phase velocities and wavelengths of stability calculations fit well with the experimental results. Concerning the group velocity, significant differences appeared in direction and magnitude. The traveling waves were found to be coherent at least over a distance of two CF vortex wavelengths. However, the question of wave front curvature could not be answered with the present sensor array.

References

[1]Gregory, N., Stuart, J. T., and Walker, W. S., "On the Stability of Three-Dimensional Boundary Layers with Application to the Flow due to a Rotating Disk," *Philosophical Transactions of the Royal Society of London, Series A: Mathematical and Physical Sciences,* Vol. 248, July 1955, pp. 155–199.

[2]Gray, W. E., "The Nature of the Boundary Layer Flow at the Nose of a Swept Wing," Royal Aircraft Establishment, RAE TM Aero 256, Farnborough, England, UK, June 1952.

[3]Arnal, D., Habiballah, M., and Coustols, E., "Théorie de l'instabilité laminaire et critères de transition en écoulement bi et tridimensionel," La Recherche Aérospatiale, No. 2, 1984, pp. 123–143.

[4]Malik, M. R., and Poll, D. I. A., "Effect of Curvature on Three-Dimensional Boundary-Layer Stability," *AIAA Journal,* Vol. 23, No. 9, 1985, pp. 1362–1369.

[5]Dallmann, U., and Bieler, H., "Analysis and Simplified Prediction of Primary Instability of Three-Dimensional Boundary-Layer Flows," AIAA Paper 87-1337, June 1987.

[6]Meyer, F., and Kleiser, L., "Numerical Investigation of Transition in 3d Boundary Layers," *Proceedings of the AGARD Symposium on Fluid Dynamics of Three-Dimensional Turbulent Shear Flows and Transition* (Cesme, Turkey), AGARD, France, 1988, p. 428.

[7]Poll, D. I. A., "Three-Dimensional Boundary Layer Transition via the Mechanisms of 'Attachment Line Contamination' and 'Cross Flow Instability,'" *Laminar-Turbulent Transition,* edited by R. Eppler and H. Fasel (IUTAM Symposium, Stuttgart, Germany), Springer-Verlag, Berlin, 1979, pp. 253–262.

[8]Saric, W. S., and Yeates, L. G., "Experiments on the Stability of Crossflow Vortices in Swept-Wing Flows," AIAA Paper 85-0493, Jan. 1985.

[9]Nitschke-Kowsky, P., "Experimentelle Untersuchungen zu Stabilität und Umschlag dreidimensionaler Grenzschichten," DFVLR-FB 86-24, Göttingen, Germany, June 1986.

[10]Kachanov, Y. S., and Tararykin, O. I., "The Experimental Investigation of Stability and Receptivity of a Swept-Wing Flow," *Laminar-Turbulent Transition,* edited by D. Arnal and R. Michel (IUTAM Symposium, Toulouse, France), Springer-Verlag, Berlin, 1990, pp. 499–509.

[11]Bippes, H., Müller, B., and Wagner, M., "Measurements and Stability Calculations of the Disturbance Growth in an Unstable Three-Dimensional Boundary Layer," *Physics of Fluids,* Vol. 3, No. 10, 1991, pp. 2371–2377.

[12]Arnal, D., and Juillen, J. C., "Three-Dimensional Transition Studies at ONERA/CERT," AIAA Paper 87-1335, June 1987.

[13]Dagenhart, J. R., Saric, W. S., Hoos, J. A., and Mousseux, M. C., "Experiments on Swept Wing Boundary Layers," *Laminar-Turbulent Transition,* edited by D. Arnal and R. Michel (IUTAM Symposium, Toulouse, France), Springer-Verlag, Berlin, 1990, pp. 369–380.

[14]Bippes, H., and Nitschke-Kowsky, P., "Experimental Study of Instability Modes in a Three-Dimensional Boundary Layer," *AIAA Journal,* Vol. 28, No. 10, 1990, pp. 1758–1763.

[15]Mangalam, S. M., Maddalon, D. V., Saric, W. S., and Agarwal, N. K., "Measurements of Crossflow Vortices, Attachment-Line Flow, and Transition Using Microthin Hot Films," AIAA Paper 90-1636, June 1990.

[16]Müller, B., "Experimentelle Untersuchung der Querströmungsinstabilität im linearen und nichtlinearen Bereich des Transitionsgebietes," Deutsche Forschungsanstalt für Luft- und Raumfahrt e.V. DLR-FB 90-09, Göttingen, Germany, Feb. 1990.

[17]Ludwieg, H., "Ein Gerät zur Messung der Wandschubspannung turbulenter Grenzschichten," *Ingenieur Archiv,* Vol. 17, 1949, pp. 207–218.

[18]Deyhle, H., and Bippes, H., "On the Receptivity of Cross-Flow Instability in 3-d Boundary-Layer Flows," presentation at the First European Fluid Mechanics Conf., Cambridge, England, UK, Sept. 1991.

[19]Nayfeh, A. H., and Padhye, A., "Relation Between Temporal and Spatial Stability in Three-Dimensional Flows," *AIAA Journal,* Vol. 17, No. 10, 1979, pp. 1084–1090.

[20]Wagner, M., "Lineare Stabilitätsanalyse zum DLR-Transitionsexperiment in dreidimensionalen Grenzschichtströmungen," Deutsche Forschungsanstalt für Luft- und Raumfahrt e.V. DLR IB 221-90 A 04, Göttingen, Germany, March 1990.